Bulletin of Earthquake Engineering
https://doi.org/10.1007/s10518-025-02272-0

ORIGINAL ARTICLE

Numerical simulation of the shake-table response of a U-shaped RC wall using the Applied Element Method

Andrea Orgnoni[1] · Rui Pinho[2] · Ryan Hoult[3] · João Pacheco de Almeida[3]

Received: 23 May 2025 / Accepted: 25 August 2025

Abstract
The Applied Element Method (AEM) has in the recent years been increasingly employed to assess the failure mechanisms developed by structures subjected to dynamic loading. However, its use in the detailed estimation of local response parameters such as strains, curvature, and other localised deformations of reinforced concrete (RC) elements under seismic excitation, is not common. In this context, we explore the feasibility of using the AEM to reproduce, in blind-prediction fashion, the recent shake-table axial-flexural-torsional response of a 40-ton half-scale reinforced concrete U-shaped wall specimen. The accuracy of the adopted modelling approach in capturing the experimentally observed translational-torsional structural response of the tested structure is demonstrated through the comparison between numerical predictions, obtained before the publication of the test results (and thus without post-test model improvements), and the experimental measurements, considering both global and local response quantities. On a somewhat separate note, this study also examined the manner in which currently available formulations are capable of estimating residual drifts in RC walls, and proposes an updated equation that is shown to predict, with a good degree of accuracy, post-earthquake shaking residual displacements for this type of structures.

Keywords Applied Element Method · U-shaped RC walls · Nonlinear dynamic response

✉ Rui Pinho
rui.pinho@unipv.it

Andrea Orgnoni
andrea.orgnoni@iusspavia.it

Ryan Hoult
ryan.hoult@uclouvain.be

João Pacheco de Almeida
joao.almeida@uclouvain.be

[1] University School for Advanced Studies, IUSS Pavia, Pavia, Italy

[2] Department of Civil Engineering and Architecture, University of Pavia, Pavia, Italy

[3] Institute of Mechanics, Materials and Civil Engineering, Louvain-la-Neuve, UCLouvain, Belgium

Published online: 19 September 2025

1 Introduction

Reinforced Concrete (RC) structural walls are frequently used as the main lateral load-resisting system in many building typologies (RC, steel, timber, etc) to provide lateral stiffness and withstand forces and displacements caused by wind and seismic activity. In some regions with low-to-moderate seismic risk, a single core wall is often employed, tasked with resisting both lateral and torsional forces acting on the building (e.g., Hoult et al. 2015). In such cases, the combined effects of flexural and torsional stresses may lead to premature failure of the wall, with limited ductility. Even if failure is not reached, significant post-earthquake residual displacements may trigger the need for expensive repairs or potentially the demolition and reconstruction of the entire structure (Hoult 2022). Further, past experimental campaigns (Beyer et al. 2008, Constantin and; Almeida et al. 2016; Hoult et al. 2020, 2023) have highlighted the susceptibility of some types of U-shaped concrete walls, mainly characterised by a small flange thickness, to global and local instabilities such as out-of-plane failure and rebars buckling, the occurrence of which causes a drastic reduction in the capacity of the structural element, especially for structures subjected to bidirectional loading.

In this context, increasingly refined numerical models of RC walls have been developed in recent years to study in-depth both the global response, such as the hysteretic force-displacement behaviour and residual deformations (or residual drift), as well as the local response, such as curvature profiles and the strain-stress state within individual components, e.g., reinforcement bars. Some of the current modelling methodologies are also capable of accurately simulating the damage state and type of failure of these structural elements, albeit with a non-negligible computational effort. The cyclic and dynamic response of RC walls has been extensively modelled over the recent decades, both from the macroscopic (macro-element models) and microscopic (Finite Element, FE) points of view. Among the former numerical approach, one may find e.g., the Multiple-Vertical-Line-Element-Model (MVLEM) by Isakovic and Fischinger et al. (2019), and the Nonlinear Beam Truss Model (BTM) formulated by Panagiotou et al. (2012); these approaches were frequently applied to the nonlinear analysis of RC walls, for example by Janevski et al. (2023) and Janevski and Isakovic (2024) on the MVLEM modelling of U-shaped walls using the computer program OpenSees (Mazzoni et al. 2006), and by Hoult et al. (2023), who instead applied the BTM with the software SeismoStruct (Seismosoft 2025).

The numerical modelling of RC wall behaviour has also been extensively carried out through the employment of various micro-modelling techniques. One of the most widely used is the Modified Compression Field Theory (MCFT, Vecchio and Collins 1986) and the Disturbed Stress Field Theory (DSFM, Vecchio 2000), which have been extensively employed in the modelling of RC walls by several researchers using computer programs VecTor2 (Wong et al. 2013) and VecTor3 (ElMohandes and Vecchio, 2013). Examples of such modelling endeavours are e.g., the FE modelling of planar, barbelled, and flanged RC sections undertaken by Palermo and Vecchio (2007), Abdulridha and Palermo (2017) and depicted in Fig. 1a, Hoult (2019), Hoult and Almeida (2024a), as well as the 3D modelling of RC members using solid elements carried out by Hoult and Beyer (2020), and Hoult (2021), reported in Fig. 1b. Recently, Wang et al. (2024) used VecTor4 (Hrynyk 2013; Hrynyk and Vecchio 2019) to model the inelastic behaviour of U-shaped walls using multi-layer shell elements.

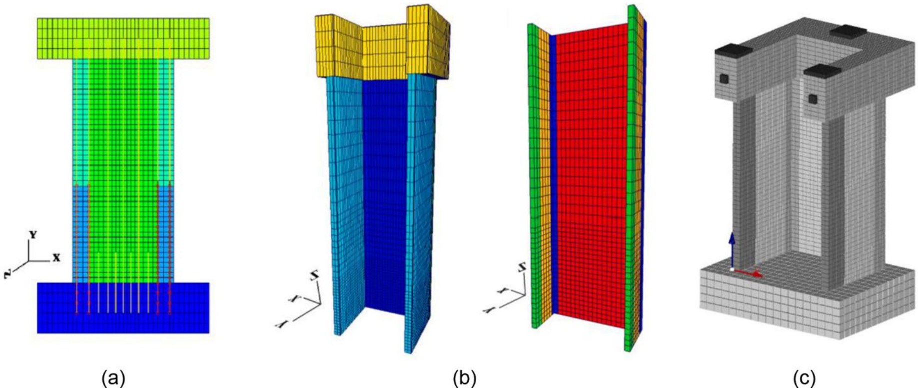

Fig. 1 Examples of RC walls numerical modelling: (**a**) VecTor2 model developed by Abdulridha and Palermo (2017), (**b**) VecTor3 model developed by Hoult (2021), and (**c**) AEM model developed by Orgnoni and Pinho (2024)

Other RC wall micro-modelling strategies can be found in the recent literature, such as for instance the employment of beam distributed plasticity models carried out in SeismoStruct (Seismosoft 2025) by Almeida et al. (2016), as well as the use of shell elements to represent concrete and rebars in Diana (2016), by Dashti et al. (2018), Belletti et al. (2018), Rosso et al. (2022). The HybriDEM method (Bouckaert et al. 2024, 2025) combines instead Finite and Discrete Element formulations, constituting a promising modelling strategy for the future.

An alternative micro-modelling approach seldomly used in recent years for the static analysis of RC walls, and never used for the dynamic analysis of these structures, is the Applied Element Method (AEM). Examples of such modelling exercises can be found in Meguro and Tagel-Din (2001) and Cismasiu et al. (2017), who modelled a planar RC wall subjected to, respectively, cyclic and monotonic loading. Orgnoni and Pinho (2024) also employed the AEM to numerically simulate, for the first time, the flexural-torsional experimental response of two U-shaped walls (Fig. 1c) tested under cyclic loading by Hoult et al. (2023).

Regarding the numerical simulation of the dynamic behaviour of, specifically, non-planar RC walls, very few examples of FE numerical modelling can currently be found in the literature, partly due to the scarcity of shake-table experimental campaigns on these structural elements (Ile et al. 2002). At the time of writing, and to the authors' knowledge, only Payen (2023) and Hoult and Almeida (2024a), have thus far reported the modelling of the shake-table response of a U-shaped wall, respectively adopting the BTM approach, using SeismoStruct, and the MCFT framework with VecTor3. In the current study, a numerical model of a U-shaped wall scaled specimen (UWS1) tested experimentally by Hoult et al. (2025) is developed using the Applied Element Method, whose major advantages are the simplicity in modelling and the accuracy of the results with a reasonable computational effort. This methodology, although widely used in the modelling of the response of RC structures under dynamic conditions (e.g., Tagel-Din and Meguro 2000; Grunwald et al. 2018; Malomo et al. 2020; Scattarreggia et al. 2022) has not been previously employed to reproduce the shake-table nonlinear dynamic response of planar or non-planar RC walls;

recently, a number of application of the AEM on the numerical modelling of RC walls were reported in Orgnoni (2025).

In the subsequent sections of this manuscript, therefore, we proceed with a brief overview of the adopted modelling approach, the AEM, followed by the description of the test specimen and its model. Subsequently, the numerical results, obtained before the undertaking of the test, are compared with their experimental counterparts, both at the global and local scales. Selected numerical and experimental results are also used to propose an update to an existing empirical formulation for the prediction of residual displacements, given imposed structural drift, for this type of structural elements. In conclusion, potential future improvements in the numerical modelling of non-planar RC walls using the AEM formulation are suggested.

2 Brief overview of the Applied Element Method

The Applied Element Method (AEM) combines the strengths of the continuous FE formulation with the advantages of discrete element methods. It was developed in 2001 by Meguro and Tagel-Din (2001) and employed successfully to perform nonlinear analysis of RC structures (e.g., Malomo et al. 2020; Scattarreggia et al. 2022; Orgnoni and Pinho 2024). The underlying principle of the AEM is to model a structure as an assembly of small, rigid units with six degrees of freedom, connected along their surfaces by zero-thickness spring layers, as depicted in Fig. 2a. In this approach, material properties are concentrated in the springs location, so stresses and strains are primarily calculated at these spring locations, unlike the Finite Element Method (FEM), where deformations are computed within the elements.

The interface springs are defined by both normal stiffness $k_n = Edt/L$ and shear stiffness $k_{sx\text{-}sy} = Gdt/L$, where E and G represent the Young's modulus and shear modulus, respectively. These stiffness values fully describe the stresses and deformations within a specific unit volume dV (the 3D region defined by $d \cdot t \cdot L$, where d is the distance between adjacent springs, and t and L are the thickness and length of the element). Together, these springs render the entire assembly deformable.

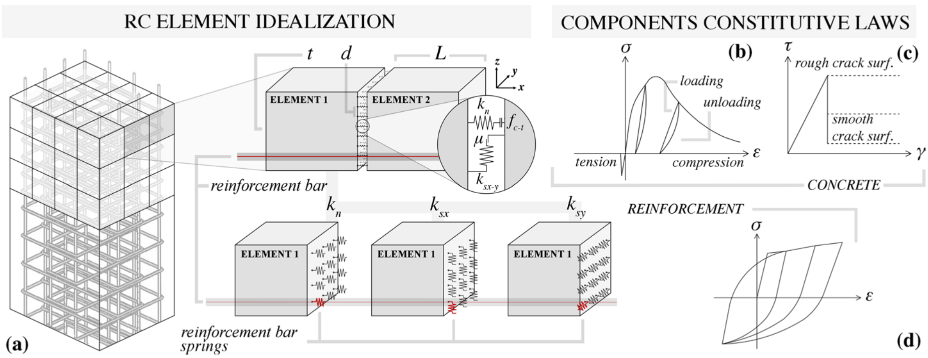

Fig. 2 (**a**) AEM modelling of RC assemblies, (**b**) material models for concrete under uniaxial cyclic tension-compression and (**c**) shear-compression loading, (**d**) constitutive law for steel reinforcement (Malomo et al. 2020)

For reinforced concrete (RC) structures, as illustrated in Fig. 2a, additional springs representing the reinforcement bars are introduced, in addition to the concrete matrix, with appropriate constitutive properties and stiffness values. However, this modelling technique does not account for the interface between reinforcement and concrete, thereby limiting the ability to capture bond-slip behaviour. To model this interaction, the reinforcement bars should be explicitly represented, and the springs connecting the rebars with surrounding concrete units defined to appropriately account for the bond-slip properties.

In the post-cracking response phase, the elastic parameters of the springs are updated based on the constitutive material laws, adjusting their stiffness and strength at each loading step to reflect the evolving damage.

In the version of the AEM-based software used in this study – Extreme Loading for Structures (ASI - Applied Science International 2021), the Maekawa and Okamura (1983) model (Fig. 2b) simulates the response of concrete under uniaxial cyclic tension-compression loading; ELS material models, in the used software version, only consider one-dimensional states of stress and hence the confinement provided by the reinforcement layout is not considered (Grunwald et al. 2018). To account for this feature, as it was done in this study (Sect. 4.2), user defined materials must be defined. Shear-compression stress states can be simulated adopting a simplified model (Fig. 2b). Steel rebars are modelled using the hysteretic model proposed by Menegotto and Pinto (1973), showed in Fig. 2c. The tangent stiffness of reinforcement is calculated based on the strain from the reinforcement spring, loading status (loading-unloading), and previous history of the steel spring.

The AEM offers several advantages over the FEM and DEM, among which the ease of modelling and the speed of calculation certainly stand out. The implicit integration scheme iterations enable the use of larger time steps compared to explicit approaches mentioned above, and the absence of in-cycle Newton-Raphson type allows to avoid continuous, time-consuming, inversions of the stiffness matrix (although at the cost of having to adopt a smaller step discretisation).

As described above, the implementation of the mesh and reinforcement layout is extremely simple and accurate; the AEM formulation, which does not require nodal connectivity (which is instead necessary for the FEM), allows the connection of various elements of distinct dimensions without the need for mesh transitions.

A comprehensive summary of the adopted methodology (AEM), as well as an excursus on its historical development, are available in Orgnoni (2025).

3 Description of the case-study: specimen UWS1 from Hoult et al. (2025)

3.1 Introduction

Two large-scale RC U-shaped walls were tested at the shake-table of the National Laboratory for Civil Engineering (LNEC, Lisbon, Portugal), within the framework of the ALL4wALL project, “Smart ALLoys for WALLs: towards durable structures with long service lives and minimal seismic displacements” (Hoult et al. 2025). These dynamic tests constituted also a natural continuation of the experimental program conducted previously at UCLouvain (Belgium) by Hoult et al. (2023), which involved the cyclic testing of two similar RC U-shaped walls, subjected to axial-flexural and axial-torsional loading.

3.2 Geometrical and material characteristics

The steel-reinforced specimen considered herein (UWS1), which, contrary to its companion USW2, did not contain smart alloy rebars, is depicted in Fig. 3a, and comprises, in addition to the two flanges and the web, a foundation, two intermediate slabs, and a top collar. This half-scaled core wall, with a full height, to the top of the collar, of 4.54 m, has the same cross-section and reinforcement detailing as the specimens tested under cyclic conditions by Hoult et al. (2023), with the only difference being the confinement and shear stirrup spacing, which, for these shake-table tests, was shortened from 75 mm to 50 mm and 150 mm to 100 mm, respectively.

The dimensions of UWS1 are 100 mm, 1300 mm, and 1050 mm respectively for the thickness (t_w), length of the web (L_w) and flanges (L_f). The reinforcement layout, shown in Fig. 3b, consist of 12 mm diameter rebars located in the boundary ends, 8 mm rebars in the web-flange boundary regions, while distributed 6 mm bars are evenly distributed in the web and flanges. Large masses, needed for the specimen to develop its full flexural capacity, are located at the top of the structure, as shown in Fig. 3a: a series of 1.13-ton and 0.59-ton mass blocks, stacked along four towers, are rigidly connected to the collar of the wall, for a total of 24.96 ton.

For what concerns the reference system and sign convention (depicted in Fig. 3b), necessary for the interpretation of the results reported in the following sections, positive directions are taken from North to South and from West to East.

The mechanical properties of the concrete and reinforcement were determined by means of material characterisation tests, described in Hoult and Almeida (2024a) and Hoult et al. (2025), which yielded the mean values summarised in Table 1 and Table

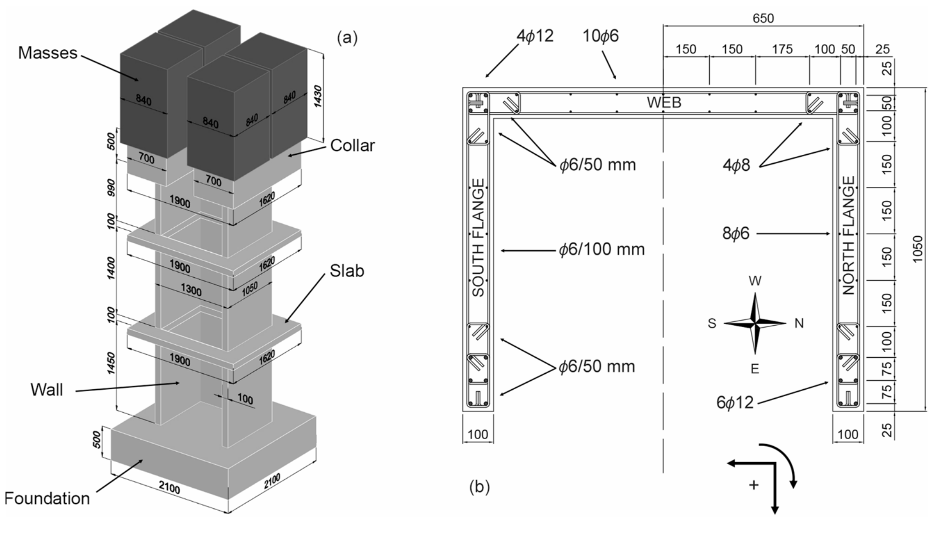

Fig. 3 Test specimen: (**a**) three-dimensional view, and (**b**) cross-section, reinforcement details, and reference system. All dimensions are in mm

Table 1 Mean values of the concrete cylinder compression strengths f'_c, expressed in MPa

Specimen	Foundation	Wall	Collar
UWS1	29.6	27.0	34.6

Table 2 Mean values of the mechanical properties of the longitudinal reinforcing bars

d_{bl} [mm]	f_y [MPa]	f_u [MPa]	ε_{su}[-]	E_s [GPa]
6	550	676	0.095	207
8	538	664	0.120	196
12	580	690	0.101	199

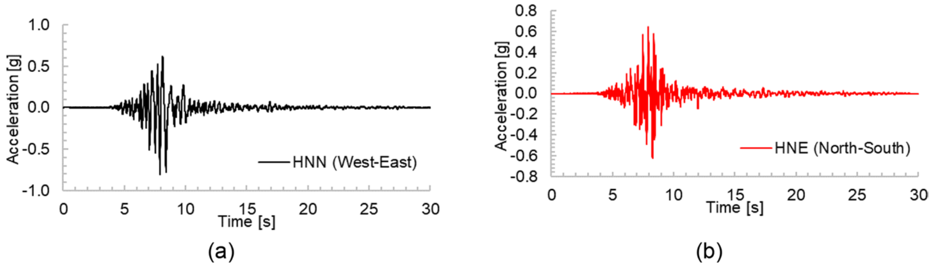

Fig. 4 Central Italy ground motion components applied on the shake table: (**a**) HNN (East-West on the shake-table). and (**b**) HNE (North-South)

Table 3 Scale factors applied to the ground motions of the M_w 6.5 central Italy earthquake event

GM	GM0	GM1	GM2	GM3	GM4	GM5	GM6	GM7	GM8
HNN	0.10	0.25	0.25	0.50	0.50	0.75	0.75	1.00	1.00
HNE	0.00	0.00	0.25	0.00	0.50	0.00	0.75	0.00	1.00

2, where d_{bl} is the rebar diameter, f_y the yield strength, f_u the ultimate strength, ε_{su} the ultimate strain and E_s the Young's modulus of the reinforcement steel.

3.3 Loading protocol

The applied loading protocol consisted in the application, under increasing scale factors (Table 2), of the two horizontal components (HNN, HNE) of a recording (station MZ04) from the Mw 6.5 Central Italy earthquake of the 30th October 2016 (Fig. 4). The HNN GM were used along the East-West (EW) shake table direction, whilst the HNE component along the North-South (NS) one. As reported in Table 3, regardless of GM0, which is considered as the test acceleration on the system, all the odd-numbered GMs (i.e., GM1, GM3, GM5, and GM7) represent a unidirectional acceleration in the EW direction, with an intensity increasing by 25% for each ground motion. Similarly, the even-numbered GMs (i.e., GM2, GM4, GM6, and GM8) represent bidirectional accelerations, adding the component in the N-S direction.

It is noted, however, that, by virtue of the half-scale nature of the test specimen, and in order for similitude laws to be respected (e.g., Pinho 2000), the ground motions had also to be scaled in time, using a "time compression" factor equal to $1/\sqrt{2}$.

3.4 Experimental instrumentation

The experimental response of the tested walls was monitored using different types of conventional instrumentation, among which: (i) linear variable differential transducer (LVDTs), employed to record the longitudinal deformation at the base of the wall, (ii) potentiometers (also referred to as string pots), used to measure the absolute displacement and rotation of the wall both in EW and NS directions at a height of 4.29 m, corresponding to the mid-depth of the collar, and (iii) accelerometers to measure acceleration along both horizontal directions, placed at different heights.

The employment of state-of-the-art optical instrumentation, namely the OptiTrack motion capture system and the Digital Image Correlation (DIC) technique, rendered possible the measurement of the 3D displacement field over a large portion of the structure (Almeida et al. 2024). A speckle pattern at the wall base, also post-processed with DIC, allowed to compute the field of 3D local strains throughout the test runs.

3.5 Observed damage – brief overview of the specimen response

The experimental response in terms of developed forces, displacements, and deformations will be discussed in Sect. 1. Herein, with a view to provide additional context to such results, a brief summary of the observed cracking is given, with the reader being directed to Hoult et al. (2025) for a more detailed account of the observed damage.

When subjected to the first four ground motions (GM1, GM2, GM3 and GM4), the structure responds essentially in “elastic-cracked” fashion; during the post-test at-rest phase, only minor hairline cracking was detected at the base of the flange and on the web. Under GM5, flexural cracks started to develop within the bottom story height at the flange boundary extremities, exacerbating existing cracks at the wall-foundation interface. Non-negligible torsion, in combination with flexural actions, were detected during the application of bidirectional ground motions GM6, with concrete crushing of a small portion located at the base of the flange-web south-west intersection being observed. Horizontal sliding along the east-west direction, was also observed at the north wall flange-foundation interface. During GM7, corresponding to 100% intensity along the east-west direction, further concrete crushing was observed in the boundary element of the south flange and in the intersection of both flanges with the web; the largest in-plane drift was recorded, reaching $\delta_{WE} = 2.71\%$.

During GM8, maximum drifts of $\delta_{WE} = 1.82\%$, $\delta_{NS} = 0.76\%$, and a rotation of $\theta_{max} = 24.7$ mrad, were recorded. Visible buckling of the longitudinal rebars at the boundary end of the south flange (Fig. 5a), as well as noticeable out-of-plane buckling of the north flange boundary element towards the inside of the wall core (Fig. 5b) developed. A non-negligible sliding at the wall-foundation interface was also observed during the final four GMs, with values of $\pm\sim 6$ mm being recorded from the OptiTrack data during GM7 and GM8. More information is available in Hoult and Almeida (2024a) and Hoult et al. (2025).

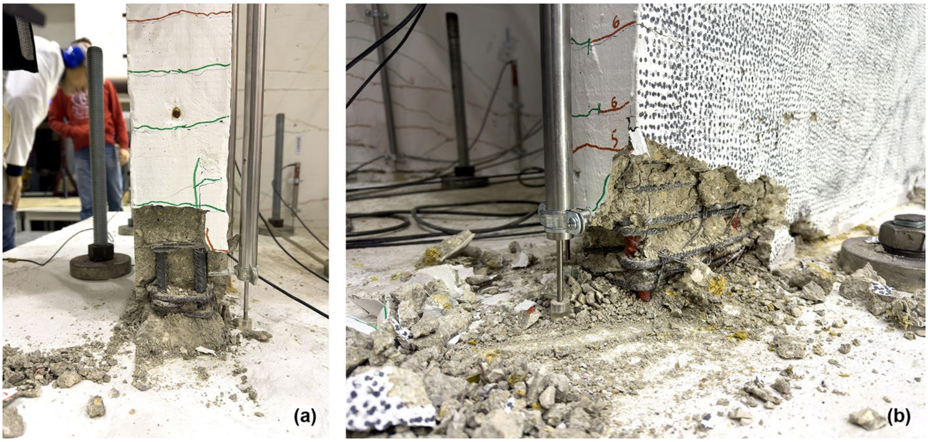

Fig. 5 Failure locations of unit UWS1 after GM8: (**a**) rebar buckling in the boundary end of south flange, and (**b**) out-of-plane buckling of the boundary end of north flange towards the inside of the wall

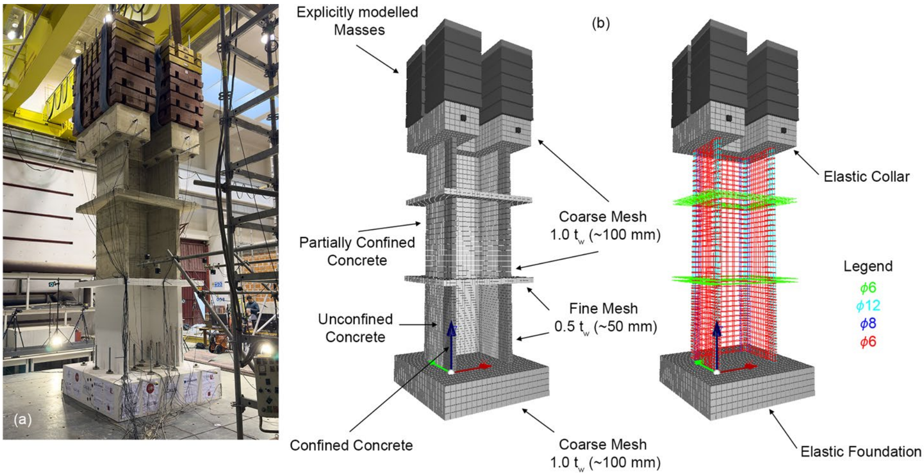

Fig. 6 (**a**) UWS1 specimen at the LNEC laboratory, and (**b**) corresponding AEM numerical modelling

4 AEM numerical modelling of test specimen response

4.1 Geometry and meshing approach

The numerical model of specimen UWS1, depicted in Fig. 6a, was implemented in the computer program Extreme Loading for Structures (ELS) (ASI 2021). The approach adopted for the definition of the structural mesh, represented in Fig. 6b, followed that described in Orgnoni and Pinho (2024), herein briefly summarised.

The foundation was modelled adopting a mesh discretisation with dimensions equal to ~100 mm per element. Regarding the web and flanges, a reasonable departure hypothesis is that the deformations will be concentrated at the first floor of the structure (between the foundation and the first slab), while the two upper floors will mainly behave in an elastic manner. For this reason, a mesh of dimension equal to 0.5 t_w (50 mm) was used for the first floor, whilst a mesh of 1.0 t_w was employed in the remaining upper portion of the wall. The discretisation of the collar was analogous to that adopted for the foundations. The intermediate slabs were modelled adopting a mesh discretisation of 0.5 t_w (50 mm). All these elements were adopted cubic elements (i.e., t=L, as depicted in Fig. 2). The top masses were implemented through the introduction of elements that have the same dimensions and density of the mass blocks employed in the test. These elements are rigidly connected between each other and also to the collar.

Overall, the numerical model features therefore 10,854 elements, each of which with twenty-five springs (5x5) implemented between the contact faces of the elements; given the blind prediction nature of this modelling effort, we have decided to adopt the meshing that had been successfully employed in Orgnoni and Pinho (2024) to reproduce the cyclic testing of two specimens practically identical to the one considered in this work.

4.2 Materials

In the same way as the AEM numerical modelling of UW1 and UW2 developed by Orgnoni and Pinho (2024), also in this case three different type of concrete materials (confined, partially confined and unconfined – see Fig. 7), were implemented in the adopted software as a user-defined material using the Mander et al. (1988) constitutive model, adopting the mechanical parameters reported in Table 1 and considering the confining effect provided by the reinforcement layout.

The Menegotto and Pinto (1973) steel constitutive model was used for the reinforcement, using the properties reported in Table 2. The reinforcement bars are assumed as being fully bonded with the concrete, and, as stated above, are represented by springs, additional to the 5×5used to represent the concrete, positioned at the actual local of the rebars. Finally, foundations and collars were characterized by an elastic material featuring the uncracked stiffness of the concrete.

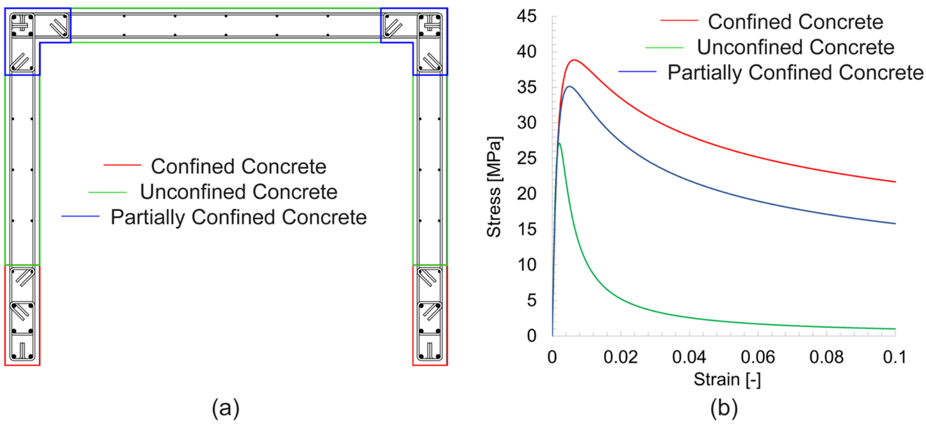

Fig. 7 (**a**) discretisation of the wall cross-section in zones with different degrees of confinement and (**b**) constitutive models adopted for concrete in compression

4.3 Loading protocol

As described in Sect. 1 and shown in Fig. 4, the shake-table loading protocol consisted in the consecutive application, for nine increasing intensity scale factors, of one or both of the two components of the record from the Mw 6.5 Central Italy earthquake of 30th October 2016, namely GM0–GM8. In the AEM numerical model, the nine dynamic analyses were also performed in consecutive fashion, so as to take into account the effects of damage accumulation. The 30-s long accelerograms that were recorded atop of the fixed foundation to the shake table during the test were used as input for the model, with a time-step of 0.005 s (200 Hz); these accelerograms were made public subsequently to the test, within the framework of the blind prediction competition organised by Hoult and Almeida (2024a). A time step of 0.005 s (200 Hz) was adopted for the numerical analysis.

5 Comparison of numerical vs. experimental results – global behaviour

This section evaluates the ability of the AEM model in replicating the global dynamic response of the U-shaped wall USW1 tested at LNEC, by comparing the numerical results, obtained before the tests execution, with experimental observations and measurements obtained from the shake table experimental campaign.

5.1 Hysteretic response

5.1.1 Comparison of the experimental results with Nonlinear Dynamic Analysis

In order to compare the numerical top displacement vs. base shear hysteretic response against its experimental counterpart, there is a need to obtain the shear force developed at the base of the test specimen. This can be estimated through the product of the total structural mass, computed as 33.6 ton (without considering the foundation), by the recorded acceleration at the (dynamic response) effective height of the wall. The latter is proposed in Priestley et al. (2018) to vary between 0.7 and 0.8 of the height of the wall, which would correspond to values of approximately 3.2 and 3.6 m. Given that the accelerometers were placed at the foundation, at the slabs (1.55 m and 3.05 m) and at the collar (4.29 m), the response acceleration time-histories at the height of 3.05 were herein employed to estimate the base shear forces developed during the test runs. It is also noted that, in order to remove signal noise, a filter was applied to the recorded acceleration time-histories using a moving average along 10 recorded values (i.e. 0.05 s).

In Fig. 8, the experimental vs. numerical results in the EW direction are reported for GMs 1 to 8, whilst in Fig. 9 the same is done for the NS direction, albeit considering only the ground motions with a perpendicular component, i.e. GM2, GM4, GM6, and GM8. From Fig. 8a to Fig. 8d (i.e. from GM1 to GM4), it is observed that in the first cycles of EW response, the numerical model does not seem to be able to capture the light energy dissipation observed in the experiment. The latter most likely arises from the hairline cracks formed at the base of the wall (see Sect. 2), which were seemingly not captured by the

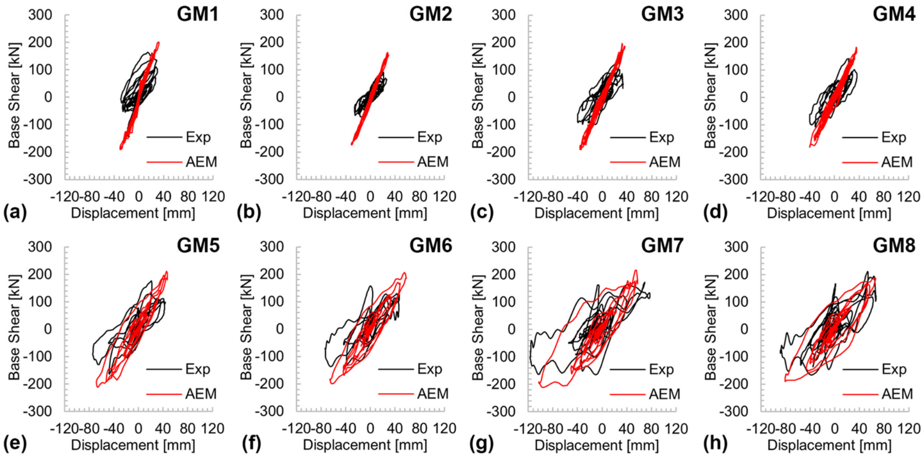

Fig. 8 Comparison between experimental and numerical hysteretic response along the EW direction

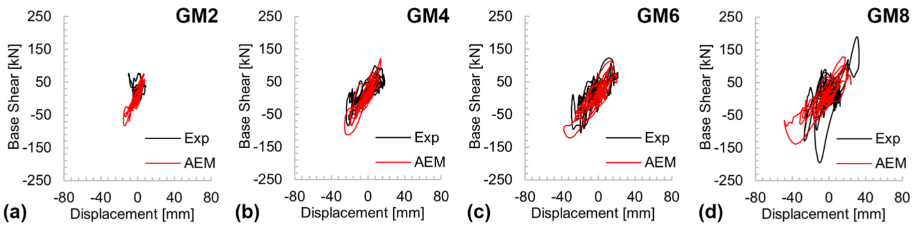

Fig. 9 Comparison between experimental and numerical hysteretic response along the NS direction, under bidirectional dynamic loading

numerical model. We note also that no equivalent viscous damping was added to the model, which, if present, could have served as a proxy for this non-captured light cracking/damage.

In the first cycles of NS response, instead, the numerical model was capable of reproducing the observed damage/energy dissipation (see Fig. 9), probably because this was instead related to cracking induced by the torsional loading, which the model was capable of simulating.

For what concerns the ground motions of higher intensity, from GM5 to GM8 (Figs. 8 to 8), where energy dissipation through material inelasticity dominates, the numerical model reproduces more closely the experimental hysteretic response.

5.1.2 Comparison of the experimental results with Pushover and Cyclic Analyses

A quasi-static reverse cyclic analysis in the EW direction, considered the one of greatest interest, was performed on a modified numerical model of UWS1, implemented following the approach proposed by Orgnoni and Pinho (2024), considering the external masses as a load, and consequently a height of the effective mass in a SDOF system of 5.1 m (Hoult et al. 2025).

Increments of 0.25% of drift, both in positive and negative direction, were applied to the structure, up to exceeding the maximum drift obtained from the dynamic experimental tests. In addition, a pushover analysis was performed, also in EW direction, by means of the application of a monotonic displacement load at the equivalent SDOF height of the structure.

In Fig. 10a, the results obtained from these two nonlinear static analyses are compared with each other, whilst in Fig. 10b they are compared also against the experimental and numerical dynamic responses, already shown in section Sect. 5.1.1, considering all eight GMs superimposed (GM0 excluded). The comparison reveals that the results from the pushover and cyclic analyses, even if obtained with a simplified model (i.e without explicitly modelling the mass block), closely envelop the dynamic numerical counterpart, which slightly overestimates the experimental dynamic response.

5.2 Displacement and rotational response histories

The numerical EW displacement time-history of the AEM model for the UWS1 specimen is illustrated in Fig. 11 and superimposed to the experimental results, obtained through the average response of two potentiometers SP10 and SP11, positioned on the most-eastern surface of the north and south collar boundary ends and at a height of 4.29 m (Hoult et al. 2025). The AEM numerical model captures well the experimental results in the final four GMs, when the intensity level is high, and the structural response is well into the inelastic range.

For GM1 to GM4 (Fig. 11a–d), the dynamic analyses results show instead a seemingly underdamped response, especially after the peak displacement for each of these initial four GMs. This could potentially have been mitigated through the addition of equivalent viscous damping to the model (albeit potentially risking an overdamped response for the final four GMs), however, herein the objective is that of showing results obtained with a model that has not been updated and fine-tuned after the experiment.

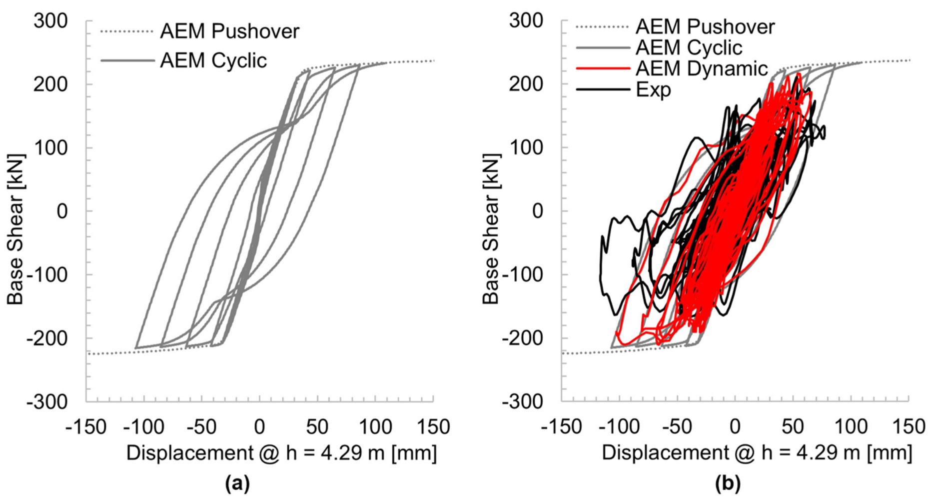

Fig. 10 (**a**) superposition of the numerical results obtained from the reverse cyclic and pushover analyses, and (**b**) comparison of the results from the pushover and reverse cyclic analyses, together with the experimental ("Exp") and numerical ("AEM dynamic") dynamic hysteretic responses

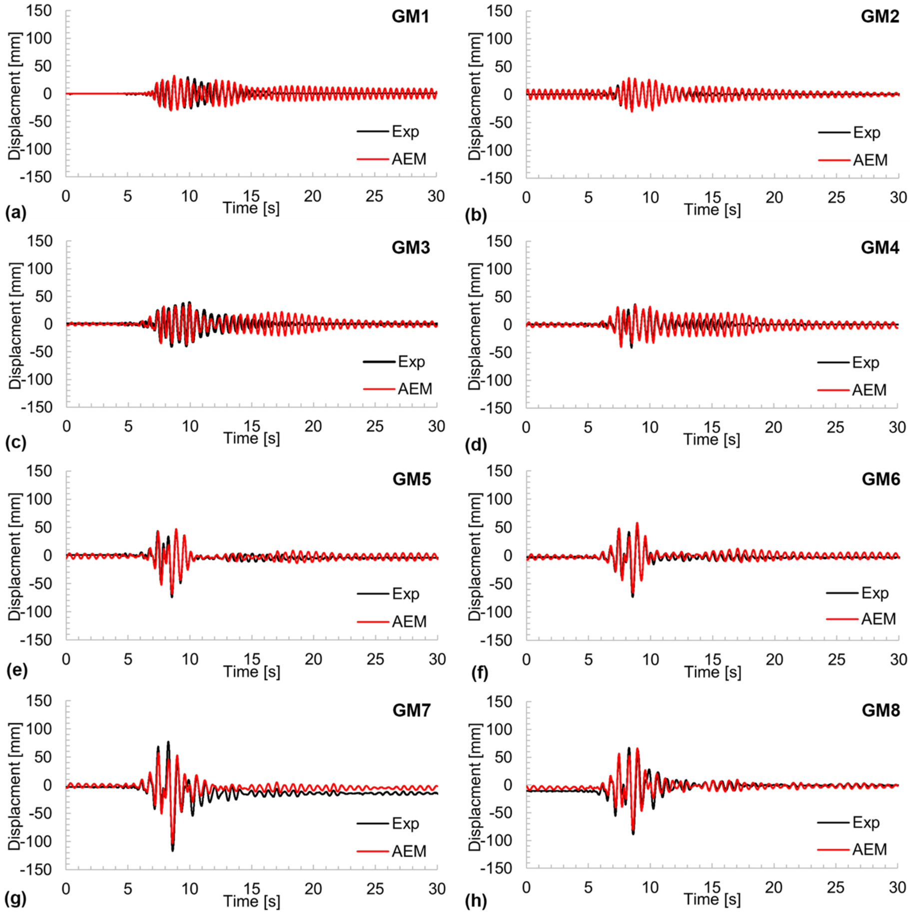

Fig. 11 Comparison between experimental and numerical displacement time-histories along the EW direction, from (a) GM1 to (h) GM8. Positive sign is toward west

Notwithstanding the low intensity underdamped response discussed above, good estimates of the peak displacement (taken as the absolute maximum displacement from the previous displacement time-histories) under every ground motion were obtained, as further confirmed in Fig. 12. The maximum relative error (i.e. the absolute value of the difference between experimental and predicted peaks, divided by the predicted value) remained inferior to 10%.

For sake of completeness, the North-South displacement and the torsional rotation time-histories are also herein scrutinised; North-South displacement were obtained as average from potentiometers SP07 and SP08, positioned at 4.29 m, while the rotations were computed by dividing the difference between East-West displacement obtained from SP10 and SP11 for their distance (1.2 m). Contrary to what was observed for the EW displacement predictions, overprediction of post-peak response histories under the first GMs is not as evident. Indeed, as gathered from Figs. 13 and 14, for all analysed ground motions (we considered only the GMs where the NS component was present, i.e. GM2, GM4, GM6 and

Fig. 12 Comparison between numerical ("AEM") and experimental ("Exp") East-West peak relative displacements (displayed in absolute value)

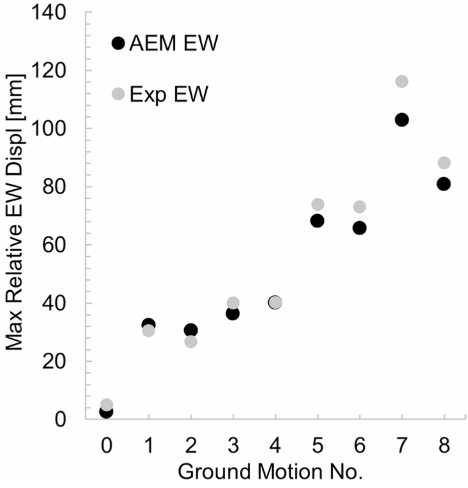

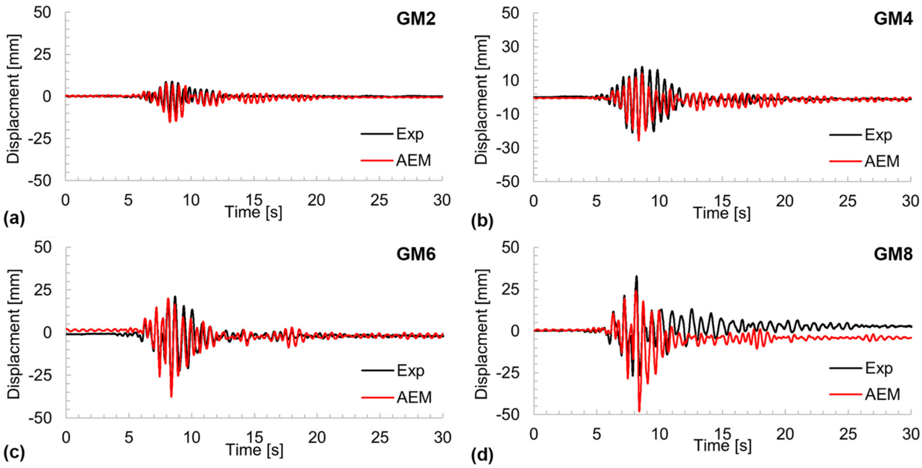

Fig. 13 Comparison between experimental and numerical displacement time-history analysis under bidirectional dynamic loading, along the NS direction: (**a**) GM2, (**b**) GM4, (**c**) GM6 and (**d**) GM8. Positive sign is towards South

GM8), the AEM numerical model captures the experimental results in a reliable manner, with exception for GM8, where some discrepancy between numerical and experimental results arise, both from the NS and rotational point of view, mainly after the peak displacement. The cause for this difference could be related to the sliding observed between the foundation and the wall, mentioned in Sect. 3, or a local failure in the wall, which reveals itself in the appearance of a large residual displacement/rotation, and which is not captured by the numerical model.

Figure 15a and Fig. 16b report the comparison of peak NS displacements and peak rotations; for the former, a good match was found, even if still with some discrepancies, which

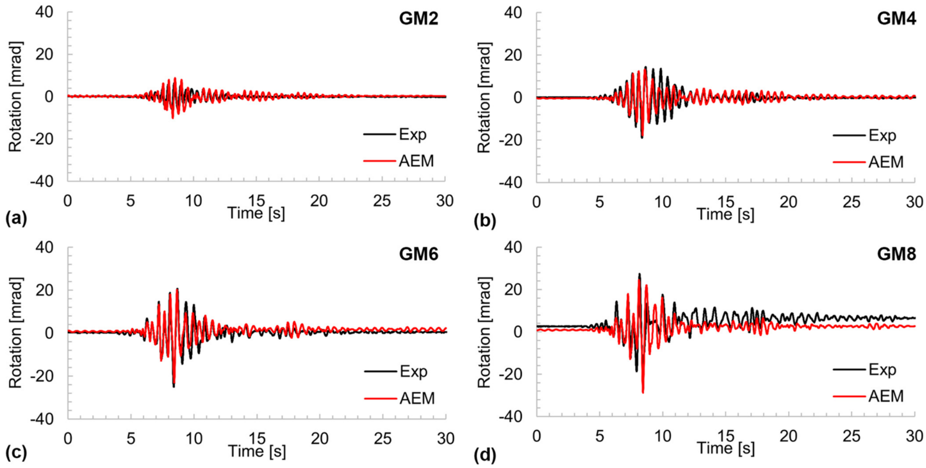

Fig. 14 Comparison between experimental and numerical torsional rotation time-history analysis under bidirectional dynamic loading; (**a**) GM2, (**b**) GM4, (**c**) GM6 and (**d**) GM8

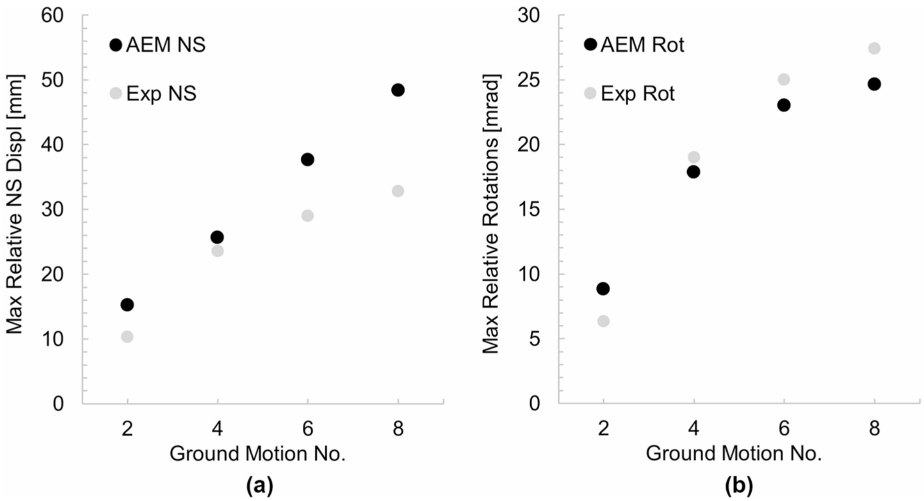

Fig. 15 Comparison between numerical ("AEM") and experimental ("Exp"): (**a**) North-South peak displacements, and (**b**) peak rotations (absolute values)

translate into a relative error on average of around 30%. For the latter, instead, the comparison is decidedly better, with an average error of about 16%.

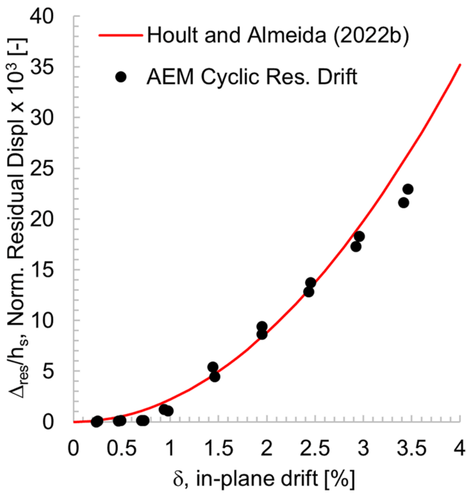

Fig. 16 Normalised *cyclic* residual displacements obtained from cyclic analysis with AEM, normalised as a function of the applied in-plane drift

5.3 Residual displacements

5.3.1 Residual displacements obtained from Cyclic Analysis

Given that in the following paragraphs the residual displacements resulting from cyclic and dynamic analyses will often be compared, to facilitate understanding, the residual displacements obtained from a nonlinear cyclic analysis will be indicated as *cyclic* residual displacements, while those resulting from nonlinear dynamic analyses, or experimentally observed from shaking table tests, are indicated as *dynamic* residual displacements.

Cyclic residual displacements obtained from the quasi-static reverse-cyclic analysis, described in Sect. 5.1.2, are reported in Fig. 16 and normalised as a function of the in-plane drift, applying the same procedure used in Orgnoni and Pinho (2024). The residual displacements are very much in line with the empirical expression (Eq. 1) developed by Hoult and Almeida (2022b) from a large database of force-displacement hysteresis curves obtained from experimental walls campaigns, that express the normalised maximum possible residual drift (Δ_{res}/h_s) as a function of the in-plane (δ) imposed on the wall planar and non-planar walls tested using quasi-static reverse cyclic analyses, is also plotted.

$$\frac{\Delta_{res}}{h_s} = 0.0022 \cdot \delta^2 \tag{1}$$

5.3.2 Residual displacements obtained from Dynamic Analysis

Figure 17a reports a comparison between experimental and numerical *dynamic* residual displacements (i.e., the displacement of the wall at rest, after the ground motion shaking) expressed for each GM. Contrary to what was observed for their peak transient counterparts (Fig. 12), in this case the differences are slightly more pronounced, especially for the final four GMs, where yielding of the rebars occurred. This discrepancy between experimental and numerical residual displacements could be linked either to the impossibility of numerical rebar slippage (as discussed, in the model the reinforcement was considered as fully

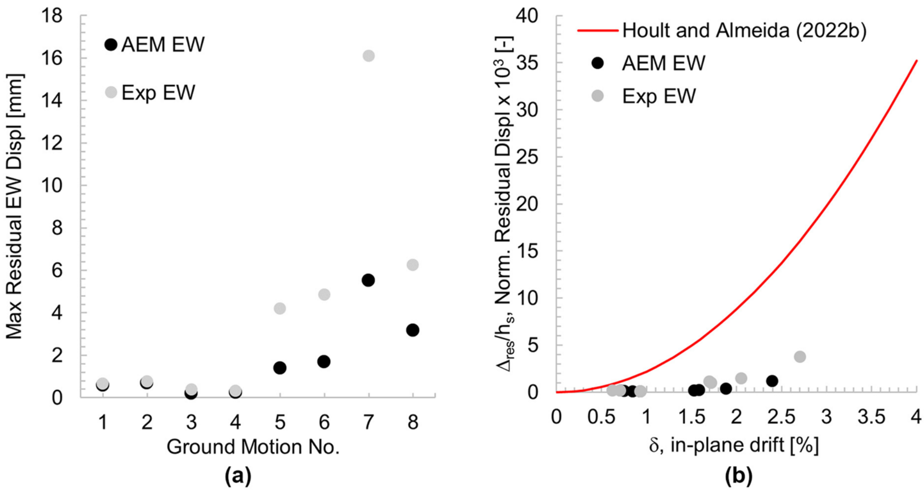

Fig. 17 Comparison between numerical ("AEM") and experimental ("Exp") East-West residual displacements, expressed in: (a) peak dynamic residual displacements vs. applied GM, and (b) normalised dynamic residual displacements vs. attained in-plane drift δ (absolute values)

bonded to the concrete), and/or, perhaps more likely, to the presence of sliding between the foundation and the wall.

In Fig. 17b, instead, the same numerical and experimental residual displacements, expressed as normalised residual displacements, are plotted against the maximum attained in-plane drift δ, adopting the same procedure used in Orgnoni and Pinho (2024). In the same figure, as done in the previous section, the empirical equation (Eq. 1) was compared to the *dynamic* residual displacements; however in this case, Eq. (1) do not envelope the *dynamic* residual displacements, obtained both experimentally and numerically, because it was derived from a large sample of quasi-static cyclic experimental tests and hence confirming that that the difference with respect to the cyclic response case, shown in the previous section, is attributable to a dynamic effect. In Sect. 6, the possible causes of this mismatch are scrutinised.

For what concerns instead the NS residual displacements and rotations (Fig. 18a and b), once again for the lower intensities (i.e. GM2 and GM4) the predictions coincide with the test observations, while for higher intensities (i.e. GM6 and especially GM8) more pronounced discrepancies are visible. These differences in displacements and residual rotations could be related to the higher stiffness used to model the collar beam, as well as the adopted G parameter (shear elastic modulus); Orgnoni and Pinho (2024) found that results of a structure subjected to a torsional loading protocol can be affected in non-negligible fashion by the parameters described above. A sensitivity analysis on the torsional stiffness, and mainly on G parameter, could have potentially helped improving results accuracy, however, as noted already, this work is focused on showing results obtained with a model that has not been updated and fine-tuned after the experiment.

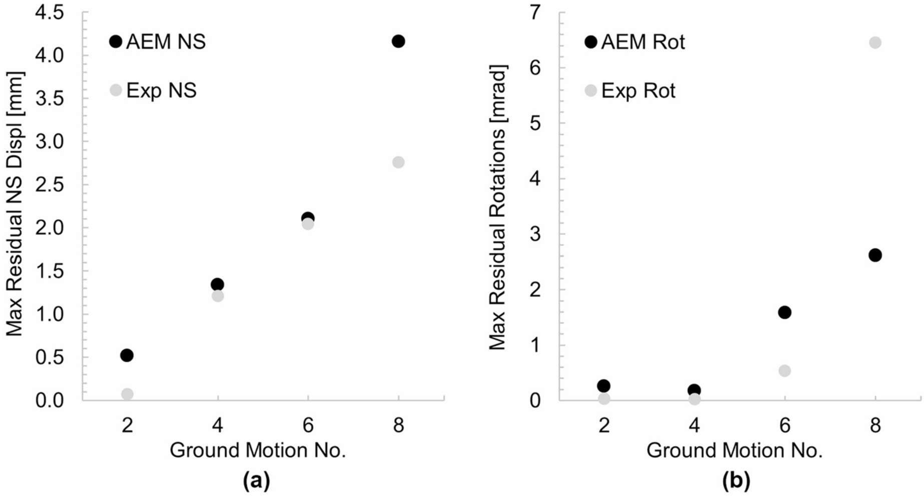

Fig. 18 Comparison between numerical ("AEM") and experimental ("Exp") results: (**a**) North-South residual displacements, and (**b**) residual torsional rotations

Fig. 19 Normalised residual displacements Δ_{res}/h_s of UWS1 as a function of in-plane drift δ (%), considering both the reverse-cyclic quasi-static response and the dynamic one. "Exp" stands for experimental measurements, while "AEM" corresponds to numerical results

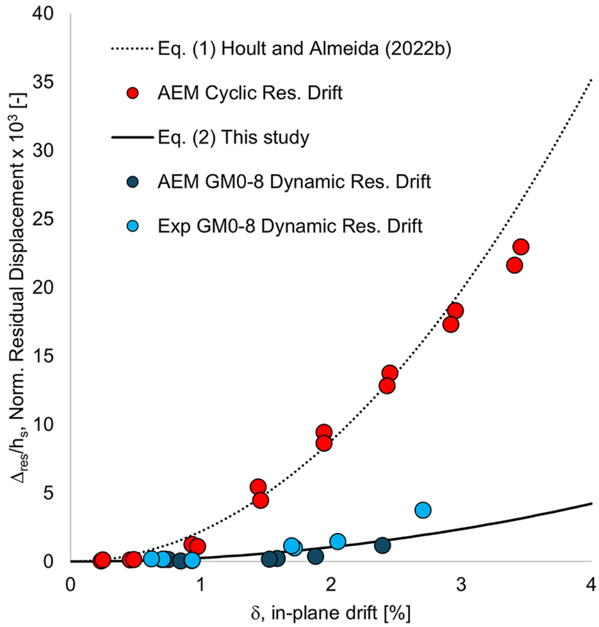

5.3.3 Discussion

Figure 19 shows the experimental normalised residual displacements, expressed in terms of the residual displacement Δ_{res} divided by the UWS1 specimen height h_s (and multiplied by 10^3) against the in-plane drift, obtained for each GM level; the measurements are compared to their numerical counterpart. These residual displacements (already reported above in Fig.

17b), labelled in Fig. 19 as *Dynamic* Residual Drift, were obtained, both experimentally and numerically, at a height of 4.29 m, at rest, when the dynamic response effectively finished. Further, in the case of the numerical analysis, this residual displacement was computed as the average displacement over the final second of the response displacement time-history, when the ground motion is practically nil, and hence the structure is essentially in free-vibration mode.

Figure 19 also displays the values of maximum possible residual displacement (*Cyclic* Res. Drift), i.e. the residual displacement obtained at a force of zero, upon quasi-static unloading from the peak displacement, on attempting to return to its original pre-load position; these values were obtained by applying the procedure suggested by Hoult and Almeida (2022b) for reverse-cyclic analyses (reported above in Fig. 16).

As one may readily observe, the maximum possible residual displacements (*Cyclic* Res. Drift) based on slow unloading from the peak displacement, computed from the quasi-static cyclic analysis described above, are quite different from the *dynamic* residual displacements, obtained both from the shake-table test results as well as from the corresponding numerical simulation. MacRae and Kawashima (1997) have shown, from a numerical study on many bilinear single-degree-of-freedom (SDOF) oscillators, that structures with positive stiffness ratios (i.e. post-elastic hardening behaviour), subjected to dynamic loading, generally oscillate about the zero displacement position and have small residual displacements compared to the peak dynamic displacement, and compared to the residual displacement obtained from a quasi-static cyclic analysis.

In this study, leveraging on the results obtained by MacRae and Kawashima (1997), a modified version of Eq. (1), intended to capture the actual residual displacement for both quasi-static cyclic and dynamic responses, is proposed (Eq. 2).

$$\frac{\Delta_{res}}{h_s} = 0.0022 \cdot \delta^2 \cdot drr \tag{2}$$

$$drr = \left| \frac{dr}{dmr} \right| \tag{3}$$

Eq. (2) sees the introduction of a new term, drr, termed *residual displacement ratio* (Eq. 3), varying between zero and one, expressed as the ratio of the residual displacement at the end of the ground motion dr (or, as mentioned above, *dynamic* residual displacement) and the maximum possible residual displacement (*cyclic* residual displacement) dmr.

MacRae and Kawashima (1997) found the average residual displacement ratio to be almost totally dependent on the stiffness ratio obtained from the enveloping bilinear approximation to the quasi-static reverse-cyclic response; other parameters, such as the earthquake record type, period of oscillator, and peak ductility do not significantly affect the average values obtained.

As depicted in Fig. 20a, the quasi-static reverse-cyclic hysteretic curve, obtained from the analysis described in the previous section, can be approximated by a bilinear curve. A stiffness ratio of r=0.15 was then calculated as the ratio of the plastic stiffness k_{pl} over the elastic stiffness k_{el}, as follows:

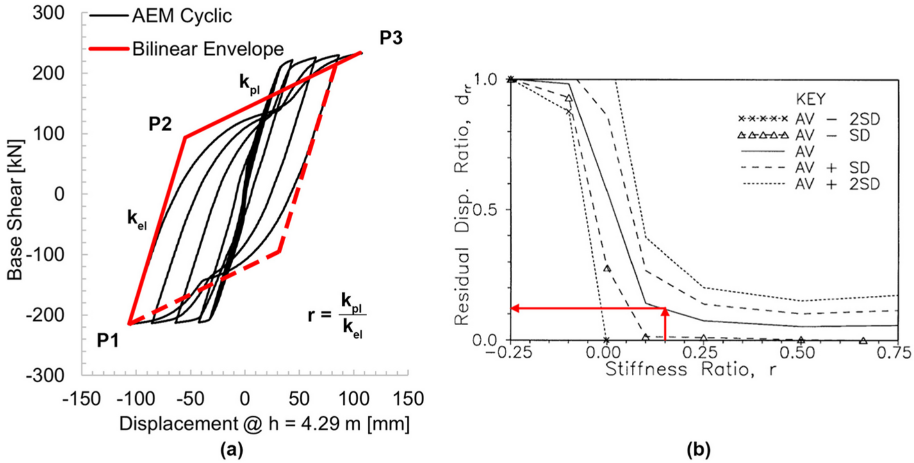

Fig. 20 (**a**) calculation of the stiffness ratio r required for the (**b**) definition of the residual displacement ratio d_{rr}, through the employment of the abacus derived by MacRae and Kawashima (1997)

$$k_{el} = \frac{(y_{P2} - y_{P1})}{(x_{P2} - x_{P1})} = 6.02 \tag{4}$$

$$k_{pl} = \frac{(y_{P3} - y_{P2})}{(x_{P3} - x_{P2})} = 0.87 \tag{5}$$

$$r = \frac{k_{pl}}{k_{el}} = 0.15 \tag{6}$$

This value was then used as input to the abacus derived by MacRae and Kawashima (Fig. 20b), and a residual displacement ratio $drr = 0.12$ was selected from the average (AV) curve.

The proposed curve (Eq. 2, plotted in Fig. 19), seems to interpolate in a quite good manner the dynamic residual displacements, both experimental and numerical. With the proposed approach, it is possible to express the *dynamic* residual displacement (i.e., after the end of the GM, when the structure comes to rest) as function of the in-plane drift attained during the dynamic response of the wall. In other words, Eq. (1) provides an estimate of the maximum residual displacements that can be compared against the results of cyclic analyses, whilst the *dynamic* residual displacements, obtained for example at the end of a nonlinear dynamic analysis, can be estimated with Eq. (2). The latter, through the definition of the residual displacement ratio drr, takes into account the dynamic/transient response of the structure. These equations may therefore be employed to check the results from cyclic/dynamic numerical analyses.

5.4 Crack patterns

The crack patterns developed on the external surfaces of specimen UWS1 were monitored in two different manners; for the North flange, Digital Image Correlation (DIC) was employed to follow crack development throughout the experiment, whilst for the South flange the cracks were visually inspected and manually annotated after each run. In the first case, the DIC allows to observe the evolution of the cracking while the structure is in motion, allowing moreover one to accurately measure the crack widths, as well as to compute the strain profile along the wall height. Conversely, manual recording of the crack state only allows the position of the cracks to be identified, with some scattered pointwise manual measurements of the crack widths at rest (i.e., when the cracks have closed). This procedure doesn't give a good idea of the largest crack widths, and make it difficult to identify cracks in general, particularly at early GM stages.

Figure 21 shows the comparison of the experimentally-obtained crack patterns, as obtained by DIC, against the principal strains in the first principal direction (1-Dir), as obtained with AEM, similarly to what has been done by Orgnoni and Pinho (2024). The comparison is performed at two different instants of GM8 (Table 4), namely at the maximum imposed negative drift along the East-West direction and at the end of the shaking.

In Fig. 21a, the numerically-computed principal strains are superimposed to the crack-pattern frame at the maximum imposed negative drift; the comparison confirms the ability

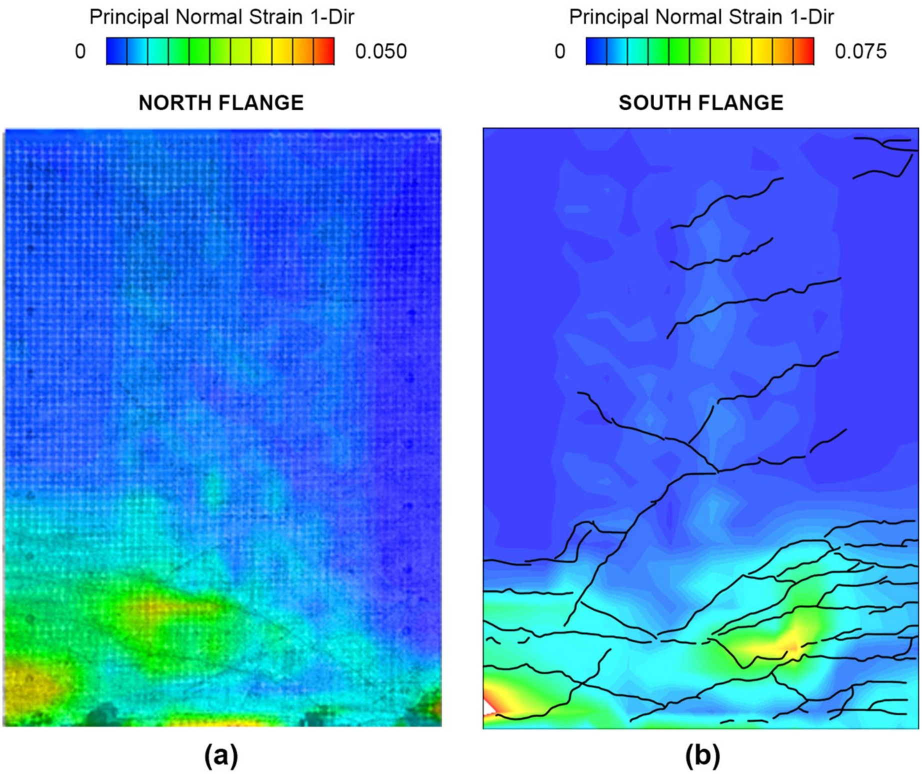

Fig. 21 Comparison between experimentally-obtained crack patterns and the numerically-derived tensile principal strains, at different times, for GM8: (**a**) at the maximum negative imposed drift along the East-West direction, and (**b**) at the end of the ground motion. (note: the graphical resolution of the cracks pattern in figure (**a**) appears of lower quality because it has been automatically produced by the DIC algorithms)

Table 4 Experimental and numerical peak drifts (δ) along the East-West direction, expressed in percentage (%) of the measured structural height (4.29 m), considered for the computation of the curvature profiles

	Observed Data		Numerical Model	
GM	δ_{west}	δ_{east}	δ_{west}	δ_{east}
1	−0.7	0.7	−0.71	0.75
2	−0.6	0.6	−0.71	0.69
3	−0.8	1.0	−0.85	0.85
4	−1.0	0.8	−0.93	0.84
5	−1.6	1.0	−1.59	1.10
6	−1.6	1.0	−1.53	1.35
7	−2.6	1.7	−2.40	1.35
8	−1.8	2.0	−1.88	1.54

of the numerical model to reliably simulate the crack distribution, which will be backed up by the comparison of the curvatures shown in the subsequent section.

Figure 21b, instead, shows the comparison of the residual crack state at the end of GM8, compared with the manual crack registration. Also in this case it is noted how the principal strains closely reproduce the crack pattern observed experimentally.

6 Comparison of numerical vs. experimental results – local behaviour

6.1 Plastic hinge length and curvature profile

Data from the OptiTrack optical system placed on the external surfaces of the North flange and the Web were used to determine the experimental curvature profiles along the EW direction; vertical displacement variation between consecutive markers were divided by the distance between the markers to obtain strain estimates, which could then be employed to compute curvature values (dividing the strain differential at a given section by the section's width).

Numerical estimates of the above parameters were also computed, and superimposed to their experimental counterparts, as reported in Fig. 22a–d for GM1 to GM4, and in Fig. 23a–d for GM5–8, for the base of UWS1, up until the first slab. The comparisons are carried out at the maximum drifts reached towards West and East directions; these values are summarised in Table 4, below.

In Figs. 22 and 23, the yield curvature profile given by the expressions for non-planar walls developed by Sullivan et al. (2012) is also indicated; it is perhaps interesting to notice that this computed yield curvature matches almost exactly the numerical curvature profiles in the upper portion of the wall (above the height of plastic rotation), while the experimental ones are well interpolated.

It can be observed that the variation throughout the height of the experimental curvature is more segmented than the numerical one, as a consequence of the discrete positioning of the OptiTrack sensors (placed at a distance of ~150 mm along the wall height), compared to the finer mesh of the numerical model (50 mm). In Fig. 22 it can be gathered that the structural behaviour during the GM1 to GM4 loading stages is essentially elastic, as noted in Sect. 5.1.1; it is in fact possible, especially from the AEM results, to note how the curvature trend is linear starting from the foundation level. This is especially noticeable for GM1 and GM2 (intensity equal to 25%), while for GM3 and GM4 (intensity equal to 50%) the influ-

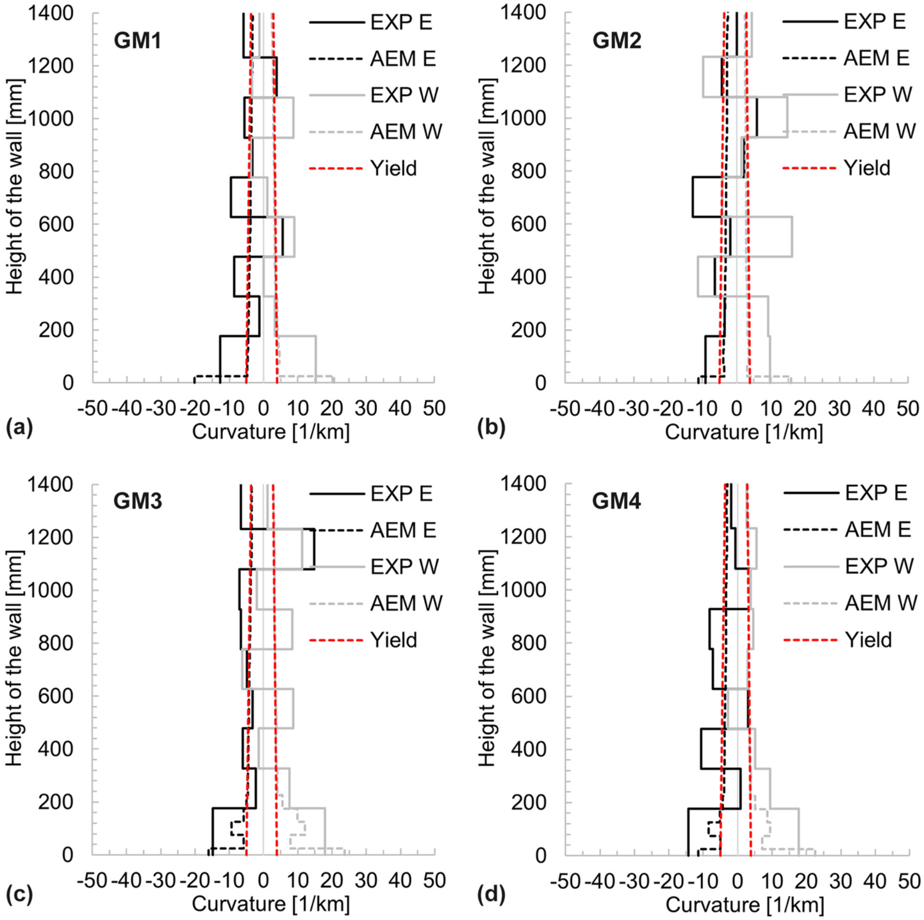

Fig. 22 Curvature profile, along the EW direction, derived experimentally ("EXP") from Hoult et al. (2025) and numerically ("AEM") for: (**a**) GM1, (**b**) GM2, (**c**) GM3, and (**d**) GM4. Results are compared both for maximum drift towards West and East directions

ence of the wall base cracks becomes more noticeable. Conversely, in Fig. 23 the curvature profile clearly depicts the non-negligible excursion into the inelastic range of response.

The experimental and numerical curvature distributions throughout the height of the wall allow one to estimate also the experimental plastic hinge length (L_p), defined as the length where post-yield curvature values were observed. The difference of the curvature shape, as well as the plastic hinge length L_p, between drifts towards West and East is evident: when the structure is subjected to a negative drift (i.e. towards West), the observed height of plastic rotations is qualitatively almost double compared to the same quantity computed when the structure is pushed towards East, both from the experimental and numerical point of view.

In Fig. 24 the equivalent plastic hinge L_p values are plotted against the maximum drift at which the structure was subjected for the GMs where the structure was subjected to inelastic deformations (GM5 to GM8), both for positive (web in tension, Fig. 24a) and

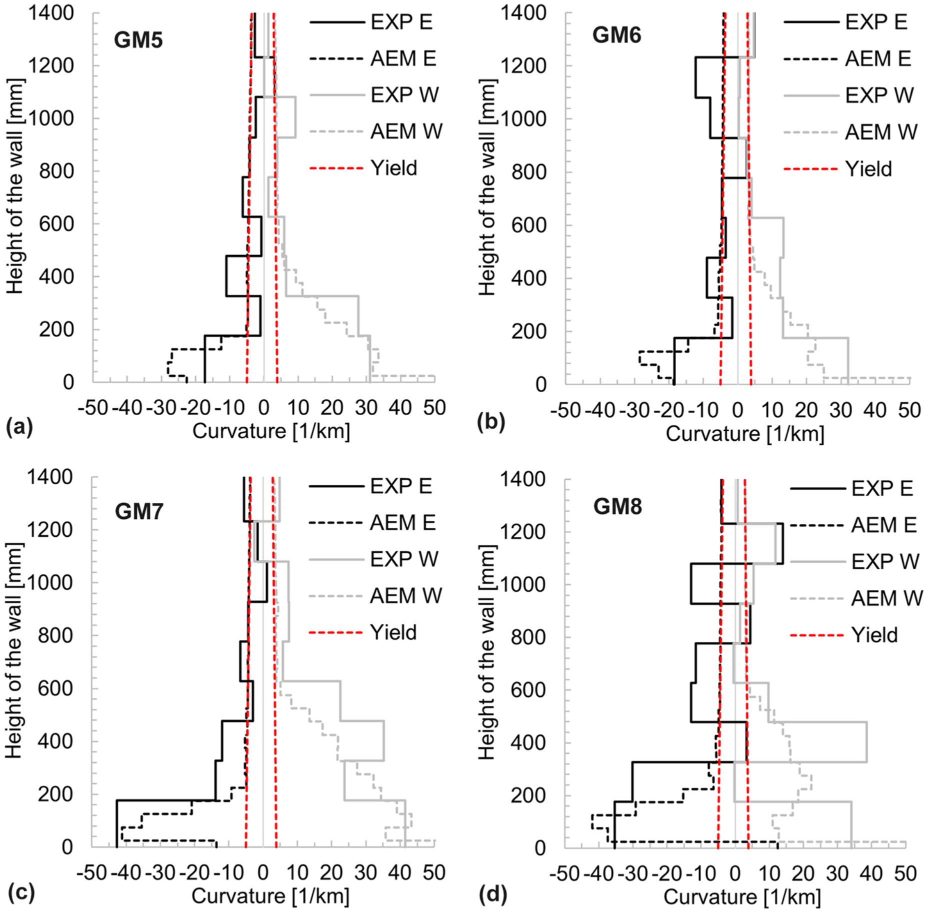

Fig. 23 Curvature profile, along the EW direction, derived experimentally ("EXP") from Hoult et al. (2025) and numerically ("AEM") for: (**a**) GM5, (**b**) GM6, (**c**) GM7, and (**d**) GM8. Results are compared both for maximum drift towards West and East directions

negative (web in compression, Fig. 24b) directions. It can be noticed that, contrary to what was observed for the nonlinear static reverse-cyclic analysis in Orgnoni (2025), here the dispersion of results is higher. This could probably be linked to the difference between the analysis (cyclic vs dynamic) and also to the experimental measuring instrumentation precision (LVDTs vs OptiTrack results). However, the comparison shows that, especially for high levels of imposed drifts, numerical and experimental L_{ps} are quite in line. It is noted also that in both directions, computed L_{ps} are generally lower than what would be expected from the empirical equations of Hoult (2022) and Eurocode 8 (2005) ; this is due to the fact that the empirical equations were obtained from databases of experimental tests mainly on cyclic (and not dynamic) analyses of walls. It is also interesting to note how the L_p values, obtained from both numerical analyses and experimental results, are different for positive drifts (web in tension) and negative drifts (web in compression); in particular, for positive

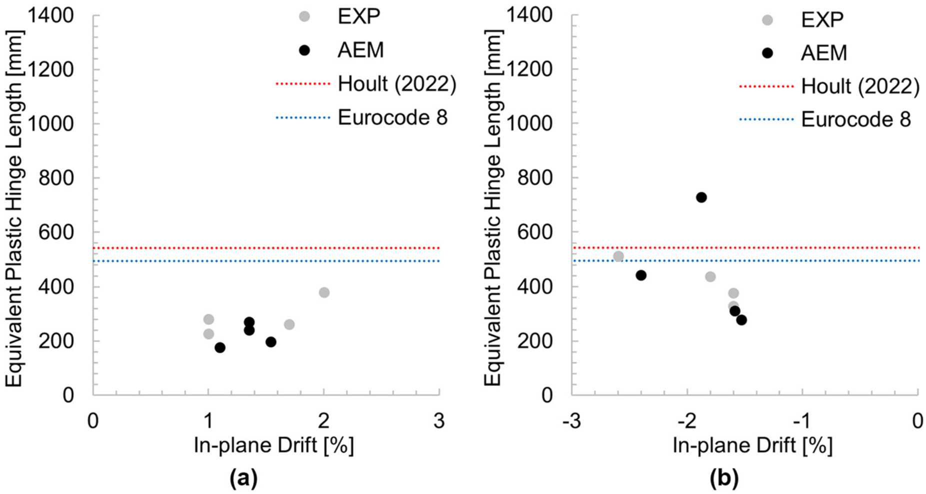

Fig. 24 Comparison of numerical and plastic hinge length L_p as a function of East-West maximum drifts for (**a**) positive drifts (web in tension) and (**b**) web in compression

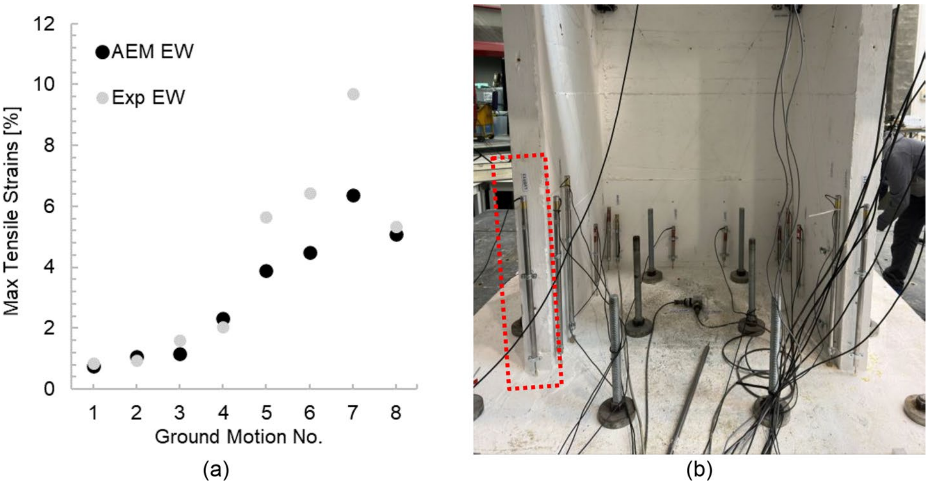

Fig. 25 (**a**) comparison of strains between the numerical ("AEM") and experimental ("exp") results at peak GM rotations, and (**b**) localisation of the LVDT used to derive the experimental results

drifts, the L_{ps} are smaller than for negative drifts. Again, the empirical equations do not reproduce these differences, as they were formulated for planar RC walls.

6.2 Longitudinal base strains

The comparison between observed and predicted strains at the base of the wall was performed using the data from the LVDT shown in Fig. 25. For this reason, the longitudinal strain is compared only locally (i.e. at the base of the South flange end), and not along

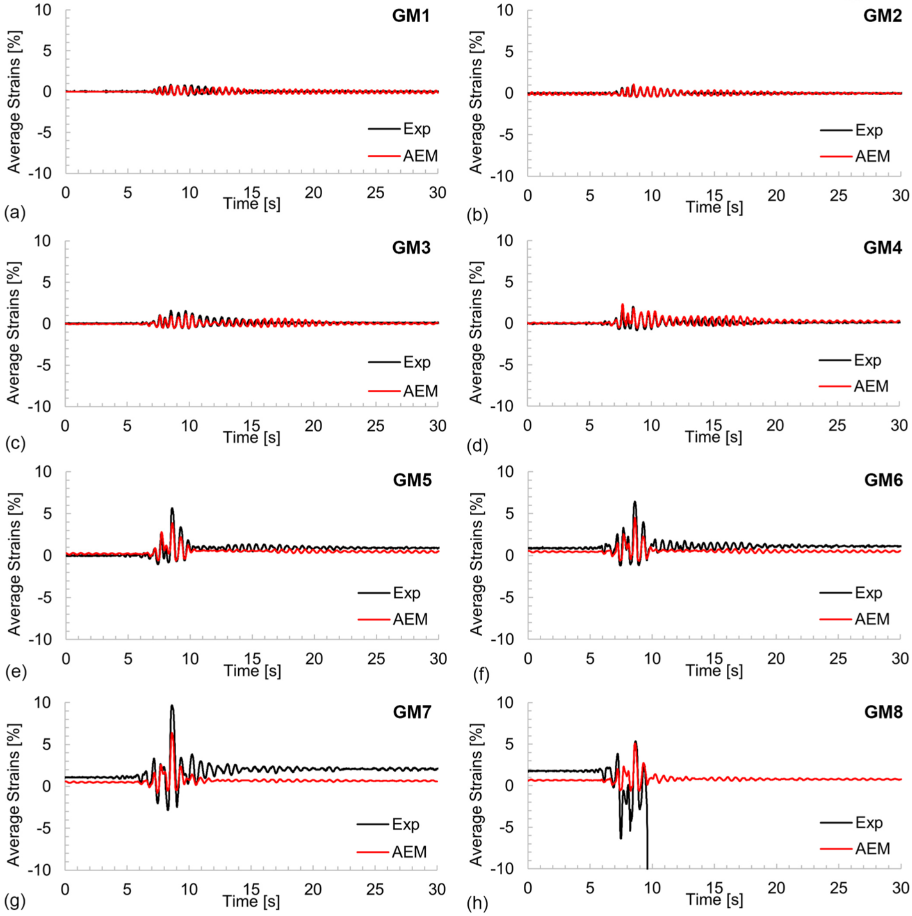

Fig. 26 Comparison between experimental and numerical average strain time-history of the south flange boundary end, from (**a**) GM1 to (**h**) GM8

the entire length of the wall. The observed stains were calculated over a gauge length of 70 mm above the foundation. The numerical counterpart was obtained by computing vertical displacements at 75 mm (this value was obviously conditioned by the adopted mesh discretisation). In Fig. 25a, the maximum values obtained for each GM are compared to the experimental counterpart. The match for the first four GMs is very satisfactory, whilst from GM5 to GM7 (GM8 is not considered due to the detachment of the LVDT) there are some non-negligible differences (average error of around 50%), most likely due to the fact that strain penetration into the foundation is not adequately captured, thus underestimating the observed strain values.

Figure 26 reports the complete tensile strain time-history. Also in this case, the AEM model was able to reproduce the general trend observed experimentally. From GM1 to GM4, as in the previous comparisons, the effect of the absence of damping is still visible, whilst from GM5 to GM8 the experimental values are consistently larger than the numerical ones (in line with Fig. 25a above).

For comparison purposes, it is important to highlight that the deviation of the time history of the experimental strains compared to the numerical ones, represented in Fig. 26h, is simply due to the detaching of the measuring instrument, caused by the spalling of the concrete at the base of the wall.

Although the AEM model was overall able to simulate this important local demand parameter at the base of the wall, the comparisons shown in Fig. 26 reveal that the strain penetration in the foundation block is not adequately captured, thus underestimating the strain values observed experimentally under the higher intensity ground motions. This is most likely due to the adoption of an elastic material model for the foundation concrete, as well as the absence of bond-slip modelling, which, in the software employed in this study, would require a computationally expensive explicit modelling of the rebars.

7 Conclusions

Reinforced Concrete (RC) structural walls are commonly employed as the primary wind and earthquake lateral load-resisting system in RC buildings, and increasingly in buildings of other structural typologies. However, the additional stresses from the combined effects of flexural and torsional actions can lead to premature low-ductility failure of RC walls, or result in significant residual displacements. Further, past experimental campaigns highlighted the susceptibility of some types of core U-shaped concrete walls, mainly characterised by a small flange thickness t_w, to certain types of global and local instabilities, such as out-of-plane failure and rebar buckling, the occurrence of which causes a drastic reduction in the displacement capacity of the structural element.

In this context, several numerical modelling approaches, both in the macroscopic and microscopic domains, have been developed in recent years to address these challenges. In this paper, the U-shaped wall UWS1, which was experimentally tested at the National Laboratory for Civil Engineering (LNEC) in Lisbon as part of the ERIES ALL4wALL project, was simulated with the Applied Element Method (AEM), with a model developed and run prior to the execution of the test. To the authors' knowledge, this corresponds to first application of AEM to the simulation of the nonlinear dynamic response of RC walls. The AEM offers several key advantages, including simplicity in modelling combined with high accuracy of results, at a reasonable computational effort. A broad range of analysis capabilities, from basic elastic static analysis to advanced explicit progressive collapse modelling, are available.

A summary of the main findings of the present investigation is given below:

- Global results for specimen UWS1 were simulated with a good degree of accuracy; the comparison of the longitudinal, transverse and rotational time histories, measured at the top of the RC structure, were simulated with relatively low error, for all the applied GM intensities. Further, the numerical residual drifts and residual rotations were in line with the observed ones, except for the higher intensities (GM7, GM8), where the effects of a non-negligible sliding at the base of the wall could have had a marked influence on the residual displacements. The comparison of the crack distribution, both at maximum drift and at rest, demonstrate the adequacy of the AEM modelling approach.
- The adopted mesh approach, although suitable for simulating the global response, char-

acterised by a complex interaction between flexural and torsional deformations, did not allow the simulation of the out-of-plane failure localised at the base of the flanges' boundary elements; more evolved material constitutive relationships and an explicit modelling of the rebars in the failure zone, together with explicit modelling of bond-slip and strain penetration, could have potentially catered for the simulation of this phenomenon.
- The analysis of a numerically-defined cyclic-loading of the structure, in the longitudinal direction, allowed one to further validate the numerical modelling, through the superposition of the results obtained from the cyclic analysis with those obtained from the dynamic runs.
- The numerical results, in terms of *dynamic* residual displacement, validated with experimental observations, allowed the updating of an empirical formulation capable of predicting the residual displacements for a structure, given an imposed peak drift value. This approach, although seemingly applicable to the results obtained from the current RC U-shaped wall tests, should be validated with other case studies.
- The comparisons of curvature profiles and time-histories of the longitudinal strains at the base of the wall further demonstrated the overall adequacy of the AEM modelling approach in modelling of RC core walls subjected to flexural-torsional behaviour, despite some limitations.

Although the results obtained, prior to the test execution, with the numerical model herein described reproduced the experimental observation in a very satisfactory manner, some improvements could be adopted to further increase the accuracy level of the simulation. A minimum value of equivalent viscous damping could perhaps be added to more correctly simulate the complete time-history response during the first elastic stages, mainly along the EW direction. Sensitivity analyses could also be performed on the mesh discretisation of the second and third floor, as well as of the collar, as carried out in Orgnoni and Pinho (2024), to further improve the torsional response simulation. The same reasoning could be made regarding the shear stiffness of the collar and slabs.

More challenging time-consuming improvements could include the wall-foundation cold-joint interface modelling to simulate the non-negligible sliding observed experimentally, or the explicit modelling of the Φ12 rebars positioned in the boundary elements of the flanges, to account both for the bond-slip behaviour and thus the strain penetration in the foundation, as well as to explicitly simulate the buckling of the rebars.

Acknowledgements The support of Prof. Andrea Penna, who kindly provided access to the AEM software used in this work, is gratefully acknowledged.

Author contributions Andrea Orgnoni: writing – original draft; conceptualisation; formal analysis; validation; resources. Rui Pinho: writing – review & editing; conceptualisation; supervision. Ryan Hoult: data curation; resources; writing – review. João Pacheco de Almeida: funding acquisition, project administration, writing – review.

Funding Open access funding provided by Università degli Studi di Pavia within the CRUI-CARE Agreement. This work is part of the transnational access project "ERIES – ALL4Wall", supported by the Engineering Research Infrastructures for European Synergies (ERIES) project (http://www.eries.eu), which has received funding from the European Union's Horizon Europe Framework Programme under Grant Agreement No. 101058684. This is ERIES publication number J7.

Data availability Not applicable.

Code availability Not applicable.

Declarations

Conflicts of interest The authors have not disclosed any competing interests.

References

Abdulridha A, Palermo D (2017) Behaviour and modelling of hybrid SMA-steel reinforced concrete slender shear wall. Eng Struct 147:77–89

Almeida JP, Hoult R, Bertholet A, Candeias P, Carvalho A, A CA, Cumunel G, Doneux C, Han Y, Isakovic T, Janevski A, Lo Feudo S, Mihaylov B, Orgnoni A, Payen B, Palermo D, Pinho R, Ribeiro F, Sousa ML (2024) Shake-table testing of two U-shaped RC walls: Overview of the project ERIES-ALL4wALL. Proceedings of the 18th world conference of earthquake engineering, WCEE2024, Milan

Almeida J, Prodan O, Rosso A, Beyer K (2017) Tests on thin reinforced concrete walls subjected to in-plane and out-of-plane cyclic loading. Earthq Spectra 33(1):323–345. https://doi.org/10.1193/101915eqs154dp

Almeida JP, Tarquini D, Beyer K (2016) Modelling approaches for inelastic behaviour of RC walls: multi-level assessment and dependability of results. Arch Comput Methods Eng 23(2016):69–100

ASI - Applied Science International (2021) Extreme loading for structures (ELS), Durham (NC), USA

Belletti B, Scolari M, Almeida J, Beyer K (2018) Validation of NLFEA of reinforced concrete walls under bidirectional loading. In proceedings of Italian concrete days 2016, Springer International Publishing (pp 32–48

Beyer K, Dazio A, Priestley MJN (2008) Quasi-static cyclic tests of two U-shaped reinforced concrete walls. J Earthquake Eng 12(7):1023–1053. https://doi.org/10.1080/13632460802003272

Bouckaert I, Godio M, Almeida JP (2024) A hybrid discrete-finite element method for continuous and discontinuous beam-like members including nonlinear geometric and material effects. Int J Solids Struct 294:112770 https://doi.org/10.1016/j.ijsolstr.2024.112770

Bouckaert I, Godio M, Almeida JP (2025) Hybrid discrete-finite element method for biaxially-discretized structures. Structures. Vol. 71. Elsevier https://doi.org/10.1016/j.istruc.2024.107954

Cismasiu C, Ramos AP, Moldovan ID, Ferreira DF (2017) Applied element method simulation of experimental failure modes in RC shear walls. Comput Concr 19(4):365–374. https://doi.org/10.12989/cac.2017.19.4.365

Dashti F, Dhakal RP, Pampanin S (2018) Validation of a numerical model for prediction of out-of-plane instability in ductile structural walls under concentric in-plane cyclic loading. J Struct Eng 144(6):04018039

Diana TNO (2016) Finite element analysis user's manual - release 10.1. Delft, Netherlands: DIANA FEA BV

ElMohandes F, Vecchio F (2013) Vector3 and FormWorks plus user manual. Department of civil engineering. University of Toronto. Retrieved from http://www.civ. utoronto.ca/vector/user_manuals/manual6.pdf

EN 1998-3:2005 (2005) Eurocode 8: design of structures for earthquake resistance—Part 3: assessment and retrofit of buildings. European committee for standardisation, Brussels, Belgium, 2005, pp 91

Fischinger M, Isaković T, Kolozvari K et al (2019) Guest ed: Nonlinear modelling of reinforced concrete structural walls. Bull Earthquake Eng 17:6359–6368. https://doi.org/10.1007/s10518-019-00715-z

Grunwald C, Khalil AA, Schaufelberger B, Ricciardi EM, Pellecchia C, De Iuliis E, Riedel W (2018) Reliability of collapse simulation-comparing finite and applied element method at different levels. Eng Struct 176:265–278. https://doi.org/10.1016/j.engstruct.2018.08.068

Hoult R (2021). Torsional capacity of reinforced concrete U-shaped walls. In Structures (vol. 31, pp 190–204). Elsevier. https://doi.org/10.1016/j.istruc.2021.01.104

Hoult R (2022) Universal plastic hinge length for reinforced concrete walls. Aci Struct J 119(4):75–83

Hoult R, Almeida JP (2022a) Tests on reinforced concrete U-shaped walls subjected to torsion and Flexure. Open Data @ UCLouvain V2. Open Data @ UCLouvain, V2, UNF:6:DvU7Ya0ZqKhhltjYY1V7Kg== [fileUNF] https://doi.org/10.14428/DVN/FDJ4EU

Hoult R, Almeida JP (2022b) Residual displacements of reinforced concrete walls detailed with conventional steel and shape memory alloy rebars. Eng Struct 256:114002. https://doi.org/10.1016/j.engstruct.2022.114002

Hoult R, Almeida JP (2024a) ERIES - ALL4wALL blind prediction competition: shake-table response of 40-ton RC U-shaped wall: summary report

Hoult R, Almeida JP (2024b) Modified compression field theory and disturbed stress field model on the simulation of the global and local behaviour of non-planar reinforced concrete walls under cyclic and dynamic loading. Bull Earthquake Eng 1–46

Hoult R, Appelle A, Almeida J, Beyer K (2020) Seismic performance of slender RC U-shaped walls with a single-layer of reinforcement. Eng Struct 225:111257. https://doi.org/10.1016/j.engstruct.2020.111257

Hoult R, Bertholet A, Almeida JP (2023) Core versus surface sensors for reinforced concrete structures: A comparison of fiber-optic strain sensing to conventional instrumentation. Sensors (Basel) 23(3):1745. https://doi.org/10.3390/s23031745

Hoult R, Beyer K (2020) Decay of torsional stiffness in RC U-shaped walls. J Struct Eng 146(9). https://doi.org/10.1061/(ASCE)ST.1943-541X.0002733

Hoult R, Correia AA, Almeida JP (2023) Beam-truss models to simulate the axial-flexural-torsional performance of RC U-shaped wall buildings. Civil Eng 4(1):292–310. https://doi.org/10.3390/civileng4010017

Hoult R, Correia AA, Bertholet A, Candeias P, Cumunel G, Doneaux C, Garnier D, Han Y, Isakovic T, Janevski A, Lo Feudo S, Orgnoni A, Payen B, Palermo D, Pinho R, Ribeiro F, Almeida JP (2025) Shake-table test on two 40-ton reinforced concrete U-shaped walls with uniaxial and bidirectional-torsional response. Earthq Spectra Submitted

Hoult RD (2019) Shear lag effects in reinforced concrete C-shaped walls. J Struct Eng 145(3):04018270. https://doi.org/10.1061/(ASCE)ST.1943-541X.000227

Hoult R, Doneux C, P AJ (2023) Tests on reinforced concrete U-shaped walls subjected to torsion and flexure. Earthq Spectra https://doi.org/10.1177/87552930231195315

Hoult R, Lumantarna E, M GH (2015) Torsional displacement for asymmetric low-rise buildings with RC C-shaped cores. In proceedings of the tenth pacific conference on earthquake engineering, Sydney Australia (pp 6–8)

Hoult R, M GH, Lumantarna E (2020) Plastic hinge length for lightly reinforced C-shaped concrete walls. J Earthquake Eng 24(7):1083–1114. https://doi.org/10.1080/13632469.2018.1453419

Hrynyk TD (2013) Behaviour and modelling of reinforced concrete slabs and shells under static and dynamic loads. PhD thesis, University of Toronto, Toronto Canada

Hrynyk TD, Vecchio FJ (2019) VecTor4 user's manual. University of Toronto, Toronto Canada

Ile N, Plumier C, Reynouard J (2002) Test program on U-shaped walls leading to model validation and implication to design. In proceedings of the 12th European conference on earthquake engineering

Isaković T, Fischinger M (2019) Assessment of a force-displacement based multiple-vertical-line element to simulate the non-linear axial-shear-flexure interaction behaviour of reinforced concrete walls. Bull Earthquake Eng 17(12):6369–6389

Janevski A, Isakovic T (2024) Blind prediction and post-experimental analysis of RC core wall's cyclic flexural response using MVLEM-FD. Bull Earthquake Eng 1–20

Janevski A, Kang JD, Isaković T (2023) Simulation of the E-defense 2015 test on a 10-storey building using macro-models. Bull Earthquake Eng 21(15):6553–6584

Lo Feudo S, Han Y, Cumunel G, Hoult R, Bertholet A, Garnier D, Candeias P, Correia AA, Pacheco de AJ (2025) Video tracking of targets for vibration measurement of large-scale structures under seismic excitation. Earthq Eng Struct Dyn https://doi.org/10.1002/eqe.4353

MacRae GA, Kawashima K (1997) Post-earthquake residual displacements of bilinear oscillators. Earthq Eng Struct Dyn 26(7):701–716

Maekawa K, Okamura H (1983) The deformational behavior and constitutive equation of concrete using the elasto-plastic and fracture model. J Fac Eng Univ Tokyo Series B 37(2):253–328

Malomo D, Scattarreggia N, Orgnoni A, Pinho R, Moratti M, Calvi GM (2020) Numerical study on the collapse of the Morandi bridge. J Perform Constr Facil 34(4):04020044. https://doi.org/10.1061/(ASCE)CF.1943-5509.0001428

Mander JB, Priestley MJN, Park R (1988) Theoretical stress-strain model for confined concrete, J Struct Eng (N Y N Y) 114(8):1804–1826. https://doi.org/10.1061/(ASCE)0733-9445,(1988)114:8,(1804)

Mazzoni S, McKenna F, Scott MH, Fenves GL (2006) Opensees command language manual. University of California, Berkeley, http://opensees.berkeley.edu/manuals/usermanual
Meguro K, Tagel-Din H (2000) Applied element method for structural analysis theory and application for linear materials. Doboku Gakkai Ronbunshu 2000(647):31–45. https://doi.org/10.2208/jscej.2000.647_31
Meguro K, Tagel-Din H (2001) Applied element simulation of RC structures under cyclic loading. J Struct Eng 127(11):1295–1305. https://doi.org/10.1061/(ASCE)0733-9445,(2001)127:11,(1295)
Menegotto M, Pinto PE (1973) Method of analysis for cyclically loaded R.C. plane frames including changes in geometry and non-elastic behaviour of elements under combined normal force and bending. IABSE symposium on resistance and ultimate deformability of structures acted on by well defined repeated loads. pp 15–22. https://doi.org/10.5169/seals-13741
Orgnoni A (2025) Accurate and computationally affordable estimation of the global and local response of RC wall cores subjected to seismic loading. Ph.D. Thesis, IUSS Pavia, Italy
Orgnoni A, Pinho R (2024) Applied element modelling of cyclic flexural and torsional response of non-planar RC walls. Bull Earthquake Eng 1–23 https://doi.org/10.1007/s10518-024-02065-x
Palermo D, Vecchio FJ (2007) Simulation of cyclically loaded concrete structures based on the finite-element method. J Struct Eng 133(5):728–738
Panagiotou M, I RJ, Schoettler M, Kim G (2012) Nonlinear cyclic truss model for reinforced concrete walls. Aci Struct J 109(2)
Payen B (2023) U-shaped reinforced concrete walls with shape memory alloys: large scale tests on LNEC-3D shake table and numerical modelling. Ecole polytechnique de Louvain, Université catholique de Louvain. Prom, Saraiva Esteves Pacheco De Almeida, João; Hoult, Ryan Correia, Antonio
Pinho R (2000) Shaking table testing of RC walls. ISET Journal Of Earthquake Technology 37(4):119–142
Priestley MJN, Calvi GM, Kowalsky MJ (2018) Displacement-based seismic design of structures - 2nd Edition, Eucentre Press, Pavia, Italy
Rosso A, A J-RL, P AJ, Beyer K (2022) Instability of thin concrete walls with a single layer of reinforcement under cyclic loading: numerical simulation and improved equivalent boundary element model for assessment. J Earthquake Eng 26(1):493–524. https://doi.org/10.1080/13632469.2019.1691679
Scattarreggia N, Salomone R, Moratti M, Malomo D, Pinho R, Calvi GM (2022) Collapse analysis of the multi-span reinforced concrete arch bridge of Caprigliola, Italy. Eng Struct 251:113375
Seismosoft (2025) SeismoStruct 2025 - a computer program for static and dynamic nonlinear analysis of framed structures. Available from https://seismosoft.com/
Sullivan T, Priestley N, Calvi GM (2012) A model code for the displacement-based seismic design of structures. DBD12
Tagel-Din H, Meguro K (2000) Analysis of a small scale RC building subjected to shaking table tests using applied element method. In proceedings of the 12th world conference on earthquake engineering, New Zealand (pp 1–8)
Vecchio FJ (2000) Disturbed stress field model for reinforced concrete: formulation. J Struct Eng 126(9):1070–1077
Vecchio FJ, Collins MP (1986) The modified compression-field theory for reinforced concrete elements subjected to shear. ACI J 83(2):219–231
Wang Z, Constantin R, Zhang S (2024) Modeling inelastic behavior of U-shaped walls using multi-layer shell element: assessment at both global and local levels. Bull Earthquake Eng 1–27
Wong P, Vecchio F, Trommels H (2013) Vector2 and formworks user manual. Department of civil engineering, University of Toronto